

High Seebeck Coefficient and Unusually Low Thermal Conductivity Near Ambient Temperatures in Layered Compound $\text{Yb}_{2-x}\text{Eu}_x\text{CdSb}_2$

Joya Cooley,¹ Phichit Promkhan,¹ Shruba Ganghopadhyay,¹ Davide Donadio,^{1,2} Warren E. Pickett,³ Brenden R. Ortiz,⁴ Eric S. Toberer,⁴ Susan M. Kauzlarich¹

1. *University of California, Department of Chemistry, One Shields Avenue, Davis, CA, 95616, USA*
2. *IKERBASQUE, Basque Foundation for Science, E-48011 Bilbao, Spain*
3. *University of California, Department of Physics, One Shields Avenue, Davis, CA, 95616, USA*
4. *Colorado School of Mines, Department of Physics, Golden, CO, 80401, USA*

Abstract: Zintl phases are promising thermoelectric materials because they are composed of both ionic and covalent bonding, which can be independently tuned. An efficient thermoelectric material would have regions of the structure composed of a high mobility compound semiconductor that provides the “electron–crystal” electronic structure, interwoven (on the atomic scale) with a phonon transport inhibiting structure to act as the “phonon–glass”. The phonon–glass region would benefit from disorder and therefore would be ideal to house dopants without disrupting the electron–crystal region. The solid solution of the Zintl phase, $\text{Yb}_{2-x}\text{Eu}_x\text{CdSb}_2$, presents such an optimal structure and here we characterize its thermoelectric properties above room temperature. Thermoelectric property measurements from 348 K to 523 K show high Seebeck values (maximum of $\sim 269 \mu\text{V/K}$ at 523 K) with exceptionally low thermal conductivity (minimum $\sim 0.26 \text{ W/m-K}$ at 473 K) measured via laser flash analysis. Speed of sound data provide additional support for the low thermal conductivity. Density functional theory (DFT) was employed to determine the electronic structure and transport properties of Yb_2CdSb_2 and YbEuCdSb_2 . Lanthanide compounds display an f -band well below ($\sim 2 \text{ eV}$) the gap. This energy separation implies that f orbitals are a silent player in thermoelectric properties, however we find that some hybridization extends to the bottom of the gap and renormalizes somewhat hole carrier properties. Changes in the carrier concentration related to the introduction of Eu lead to higher resistivity. A zT of ~ 0.67 at 523 K is demonstrated for $\text{Yb}_{1.6}\text{Eu}_{0.4}\text{CdSb}_2$ due to its high Seebeck, moderate electrical resistivity, and very low thermal conductivity.

Keywords: Zintl phase, thermoelectric material, electronic structure, DFT, low thermal conductivity, high Seebeck, solar thermoelectric, STEG, Yb_2CdSb_2 , YbEuCdSb_2

Broader context: Thermoelectric devices provide a reliable, non-toxic, solid-state solution to energy lost as waste heat. However, there are relatively few materials with high efficiency in the mid-temperature regime (200 – 500 °C), where a high thermoelectric figure of merit (zT) material could impact low grade waste heat recovery, such as in industrial processes, and small-scale power conversion, for example in mid-temperature solar thermoelectric generators (STEGs). $\text{Yb}_{2-x}\text{Eu}_x\text{CdSb}_2$, described herein, is a new addition to materials with efficient energy conversion (as indicated by the figure of merit, zT) and has potential in the optimal mid-temperature STEG operating range and results in a zT at 523 K of 0.67. The significant zT stems from the high Seebeck coefficient and extremely low thermal conductivity of this material due to its complex phonon dispersion and point scattering by defects. This system has an optimized thermal conductivity at or below its minimum theoretical value. These are initial measurements on a new thermoelectric material that has significant potential for future improvement.

INTRODUCTION

Thermoelectric (TE) generators can transform thermal energy into electrical energy. This thermal energy can come from a wide variety of sources such as vehicle exhaust systems¹ and solar radiation.² These devices work using the Seebeck effect in two dissimilar materials. Ideally, an *n*-type (electron conduction) semiconductor and *p*-type (hole conduction) semiconductor are joined electrically in series and thermally in parallel across a temperature gradient. In a semiconductor, carriers diffuse from the hot side of the gradient to the cold side and, since the carriers are charged, allow for a voltage difference to develop. When a load is connected across the two materials, electricity can flow. The maximum efficiency is governed in part by a dimensionless figure of merit, $zT (= S^2T/\rho\kappa)$. It follows that in order to achieve high efficiency, it is necessary to have a high Seebeck coefficient (S), low electrical resistivity (ρ) and low thermal conductivity (κ). Slack³ suggested that the ideal thermoelectric material would be a “phonon-glass, electron-crystal” (PGEC), in which the material conducts heat poorly, as in an amorphous glass, but can conduct electronic charge very well, as in a crystalline material.

Zintl phases,⁴ a subset of intermetallic phases combining ionic and covalent bonding, have been targeted as viable TE materials as they often intrinsically exhibit PGEC properties. Zintl phases have been studied at temperatures far above room temperature, up to ~ 1250 K, for TE power generation applications, and show great promise.⁵⁻¹⁴ $\text{Yb}_{14}\text{MnSb}_{11}$ ⁵ and variants thereof¹⁵ well illustrate the PGEC concept, with a lattice thermal conductivity reaching as low as 0.16 W/m-K combined with an electrical resistivity of less than 1.0 m Ω -cm in $\text{Yb}_{14}\text{MgBi}_{11}$.¹⁶ PGEC behavior has also been seen in other Zintl phases such as coinage-metal stuffed $\text{Eu}_9\text{Cd}_4\text{Sb}_9$,⁹ a derivative of $\text{Mg}_{3+8}\text{Sb}_2$, $\text{Mg}_{3.2}\text{Sb}_{1.5}\text{Bi}_{0.49}\text{Te}_{0.01}$,¹⁷ and clathrate $\text{Ba}_8\text{Ga}_{16}\text{Ge}_{30}$.¹⁸

Despite this progress, there is still considerable room for growth with respect to applications at lower temperatures, where there are a significant number of technologies that would benefit from the additional energy recovery from heat; for example, solar thermoelectric generators (STEGs). STEGs are an emerging technology that, much like photovoltaics, harvest energy from the sun to create electricity, but use concentrated thermal energy the sun provides rather than radiation.¹⁹ With a $zT = 1$ and hot and cold sides of temperatures 220 °C and 20 °C, respectively, STEGs can reach 8.6% efficiency.² Thus, high zT s in this temperature range are of

great consequence and more study to find thermoelectrically competitive materials in this temperature range is worthwhile.

Discovery of materials with high zT involves some intuition²⁰ and appropriate choice of structure.²¹ Semiconductors with large Seebeck coefficients at high temperature can be difficult to identify, thereby focusing research on low thermal conductivity materials. One method of enhancing zT involves striving for very low inherent κ in a material and working to further lower the lattice thermal conductivity (κ_{latt}). So-called complex structures have been linked to having low κ_{latt} because their large unit cells, use of heavy elements, and complex bonding schemes allow for significant phonon scattering, thus acting as a “phonon glass.” Some of these complex structures include clathrates and skutterudites,²² as well as Zintl phases such as $\text{Yb}_{14}\text{MnSb}_{11}$,⁵ coinage metal stuffed $\text{Eu}_9\text{Cd}_4\text{Sb}_9$,⁹ $\text{Ca}_5\text{Al}_2\text{Sb}_6$,¹¹ and nanostructured materials.^{23, 24} Despite this apparent requirement of complex structure types, phases with relatively simple layered structures have demonstrated favorable thermoelectric properties – often the layered structure plays a role in the compound’s PGEC properties. For example, NaCo_2O_4 contains CoO_2 layers, responsible for electronic conduction, while the disordered Na layer acts as a phonon scattering mechanism, allowing for κ of ~ 0.5 W/m-K at relatively low temperatures.²⁵ Bi_2Te_3 , a state-of-the-art TE material that is in commercial use today, is a layered compound whose low thermal conductivity of near ~ 0.7 W/m-K resembles that of a glass and contributes to its high figure of merit near room temperature.²⁶ Layered Zintl phases have also garnered attention – the AM_2Pn_2 ($A = \text{Ca}, \text{Sr}, \text{Eu}, \text{Yb}$; $M = \text{Zn}, \text{Cd}$; $\text{Pn} = \text{As}, \text{Sb}$) family of compounds, in the CaAl_2Si_2 structure type, has yielded a wealth of structures with low κ and high S , often resulting in impressive zT values.^{27, 28}

Herein, we have investigated the layered solid-solution $\text{Yb}_{2-x}\text{Eu}_x\text{CdSb}_2$ (Figure 1) as a potential thermoelectric material for near room temperature applications as motivated by the promising S and ρ reported for the single crystals.^{29, 30} $\text{Yb}_{2-x}\text{Eu}_x\text{CdSb}_2$ crystallizes in the polar space group of $Cmc2_1$. The structure is almost like that of Ca_2CdSb_2 except for a small distortion that destroys the center of inversion. The lack of an inversion center, which splits degeneracies compared to the higher symmetry structure, should translate into a more complex phonon spectrum and phonon-phonon interaction and thereby lower the thermal conductivity and increase the figure of merit. Compared to Ca- or Ba-based compounds the noncentrosymmetric space group is unique to this combination of Yb and Eu.²⁹ The layered structure and zig-zag

bonding of the anionic substructure are reminiscent of SnSe,^{31, 32} a phase exhibiting significant anharmonicity yielding low thermal conductivity. Therefore, one might expect anharmonicity to play a role in this structure type as well. There are two crystallographic sites in this structure for the rare earth cations, providing an additional degree of freedom. Not only does site substitution provide alloy scattering mechanism to reduce thermal conductivity, but site preferences for the two cation provide additional complexity that can tune properties. In this solid solution phase, we are substituting Eu for Yb and Eu preferentially substitutes on the interlayer (Yb1) site, shown in Figure 1. Eu will add additional *f* bands to the band structure and more importantly, may provide Eu-Sb bonding, as is the case in the coinage metal stuffed Eu₉Cd₄Sb₉ complexes,⁹ to also affect the gap or placement of the Fermi level. The structural features of Yb₂CdSb₂ combined with the high thermopower reported at room temperature²⁹ provides incentive to investigate Yb_{2-x}Eu_xCdSb₂ in order to confirm a high figure of merit phase based on the chemical intuition outlined above.

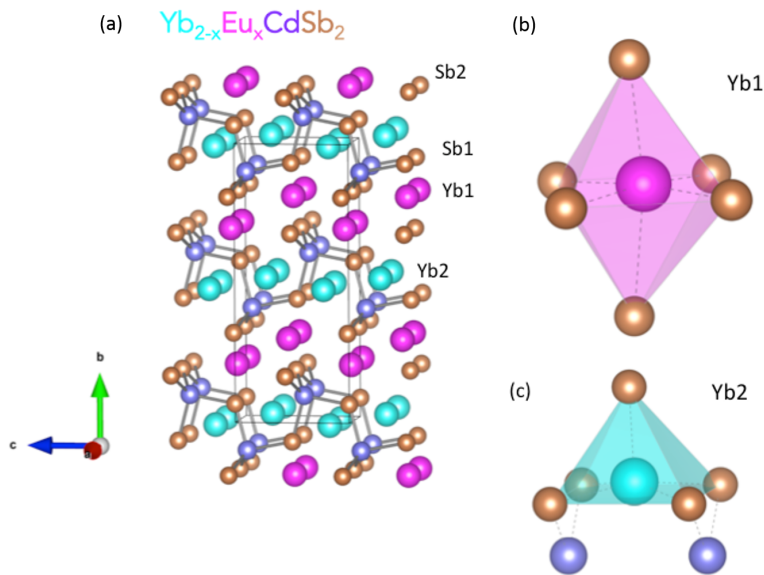


Figure 1: (a) A ball-and-stick depiction of the structures of Yb_{2-x}Eu_xCdSb₂ with one unit cell outlined. Yb, Eu, Cd, and Sb are shown as teal, pink, purple, and tan spheres, respectively. Coordination spheres of sites (b) Yb1, interlayer, and (c) Yb2, intralayer.

EXPERIMENTAL

Synthesis. Bulk samples were synthesized through a combination of mechanical milling to pulverize elements to a homogeneous powder and spark plasma sintering (SPS) to

simultaneously provide a phase pure sample and densify the powder into a pellet. Yb was filed to pieces using a metal rasp and combined stoichiometrically with cut Eu pieces, Cd shot, and Sb shot (sources: Eu metal, Stanford Materials, 99.99%; Yb pieces, Metall Rare Earth Limited, 99.99%; Cd shot, Alfa Aesar, 99.95%; and Sb shot, Alfa Aesar 99.9 %) The elements were weighed according to the following stoichiometry: 2-x Yb: x Eu: 1 Cd: 2 Sb (x = 0.3, 0.8, 1, and 1.1) to total reaction masses of 3-3.5 g. For each reaction, Yb, Cd, and Sb and two tungsten carbide (WC) balls (diameter 8.0 mm) were loaded into a 5 cm³ stainless steel ball mill, capped via a Viton O-ring with WC disks held in place by Teflon caps. The milling container was heat-sealed in two poly bags to prevent oxidation in air and placed in a SPEX 8000 M for 1 h. total in two 30 min. milling duration increments. Between increments, the milling container was transferred to a dry box, and the inside and end caps were scraped down with a metal spatula and Eu was added for the second ball milling. The resultant powder was transferred to a dry box and ground via alumina mortar and pestle to remove any large agglomerates and sieved through a 100-mesh sieve. Approximately 2.5-3 g of powder was transferred to a 12.7 mm diameter high-density graphite die (from POCO) for densification via a Dr. Sinter SPS-2050 spark plasma sintering (SPS) system (Sumitomo, Tokyo, Japan). The die was transferred to the instrument chamber, which was evacuated (below ~20 Pa) and filled with a partial pressure of Ar. The temperature was increased from room temperature to 500 °C in 15 minutes, to 600 °C in 1 minute (to prevent temperature overshoot), and remained stable for 45 minutes. When the temperature reached ~ 480 °C and compression began, the force was increased from 2 kN to 8 kN. Afterwards samples were cooled to room temperature with pressure released. Sample densities were larger than 90% of the theoretical density according to the Archimedes method.

Powder X-ray Diffraction. Ground powders of pelleted samples were loaded on a Bruker zero-background holder for powder X-ray diffraction (XRD). XRD data were collected by a Bruker D8 Advance Diffractometer with Cu K α radiation ($\lambda = 1.54060 \text{ \AA}$) with 2θ range of 20 to 80° with a step size ~ 0.02° and scan rate of 1s per step. Refinements of unit cell parameters were performed with the program FullProf.³³

Electron Microprobe Analysis. Pellet pieces from each sample were examined for phase composition by electron microprobe analysis (EMPA) using a Cameca SX-100 Electron Probe Microanalyzer equipped with a wavelength-dispersive spectrometer with 15 kV accelerating

potential and a 20 nA beam current. Small pellet pieces (~1.5 mm x 1.5 mm x 1.5 mm) were coated in epoxy and polished for analysis. The polished samples were mounted on 25 mm metal rounds with carbon tape and coated with carbon for conductivity. Characteristic X-rays generated by samples were qualitatively analyzed by wavelength-dispersive spectroscopy to determine compositions of samples using X-ray intensities of Yb, Eu, Cd, Sb as compared to calibrated standards $\text{Yb}_{14}\text{MnSb}_{11}$, EuGa_4 , Cd (metal), Sb (metal). Elemental mapping was performed to qualify element homogeneity.

Thermoelectric Property Measurement. High temperature thermal diffusivity (λ , shown in Table 2 of the ESI) was measured between 348 and 523 K on 12.7 mm diameter circular pellets using a Netzsch Laser Flash Analysis (LFA) 457 instrument. Measured thermal diffusivity was used to calculate thermal conductivity using the equation $\kappa_{tot} = \lambda\rho C_p$, where ρ is the density and C_p is the heat capacity. The density was measured using the Archimedes method, and the heat capacity was estimated using the Dulong-Petit equation $C_p = 3RN/\text{FW}$ ($R = 8.3145 \text{ J/mol-K}$, $N =$ number of moles of atoms in the formula unit, $\text{FW} =$ formula weight). Experimental heat capacity (Figure S10 in the ESI) was measured with a Netzsch Thermal Analysis DSC 404 F3 with a TASC 414/4 controller using alumina pans placed in platinum pans and the platinum furnace from 313-523 K. The Netzsch software package automatically subtracted the data and referenced against the standard (sapphire) to calculate the heat capacity values. A Linseis LSR-3 instrument was used to measure Seebeck coefficient and electrical resistivity via a standard four-probe method from 348 to 523 K under a helium atmosphere each sample. Samples were cut into bars (~12 mm x 2 mm x 2 mm) using a Buehler diamond saw and polished before measurement. The probe distance was 6 mm. The Seebeck coefficient, electrical resistivity, and thermal conductivity data were fit to fifth- or sixth-order polynomial functions to calculate zT values.

Computational Details. The present DFT-based electronic structure calculations were performed using the full-potential augmented plane wave plus local orbital method as implemented in the WIEN2K code.³⁴⁻³⁶ The generalized gradient approximation (GGA) as described by Perdew, Burke, and Ernzerhof (PBE) was used for the underlying semilocal exchange-correlation potential.³⁷ GGA+U calculations with fully localized limit are used for approximating local repulsion effects on localized atomic orbitals. In this method an on-site Hubbard repulsion U is included for the rare earth $4f$ orbitals and Cd $4d$ orbitals. The double

counting correction approach proposed by Anisimov *et al.*³⁸ and Liechtenstein *et al.*³⁹ was chosen for these highly localized orbitals and the value $U = 8$ eV, Hund's exchange parameter $J = 1$ eV were chosen for f orbitals in Yb and Eu and for Cd d orbital we applied $U = 3$ eV. Although the Cd $4d$ orbital shows minor participation near the valence edge, Flage-Larsen *et al.*⁴⁰ have shown that, in the case of YbZn_2Sb_2 , applying an on-site U for Zn d states can lead more to accurate description of electronic structure, therefore, the on-site U for Cd was employed. Also, to keep numerical consistency with magnetic YbEuCdSb_2 we applied spin polarized calculations for both Yb_2CdSb_2 , nonmagnetic ($4f^{14}$ configuration), and YbEuCdSb_2 , magnetic (Eu^{2+} , $4f^7$ configuration). The wavefunctions in the interstitial regions were expanded in plane waves up to a cutoff of $R_{\text{mt}}K_{\text{max}} = 9$ (R_{mt} is the smallest muffin tin radius of atoms and K_{max} is the maximum plane wave vector) to achieve convergence for energy eigenvalues (especially the $4f$ bands). Non-overlapping atomic sphere radii, in a.u., were chosen as 2.5 for all the constituent atoms. Plane waves with a kinetic energy cut-off 500 eV are used as basis sets and a $4 \times 1 \times 2$ k-point grid in Brillouin zone is chosen as per the Monkhorst-Pack scheme. All the pseudopotentials were calibrated with respect to the density of states obtained from all-electron WIEN2K calculations, and for both cases the same Hubbard U was applied for all rare earth $4f$ orbitals. Applied pseudopotentials have the following valence configurations: $5s^2$, $5p^6$, $4f^{14}$, $6s^2$ for Yb, $5s^2$, $5p^6$, $4f^7$, $6s^2$ for Eu, $4d^{10}$, $5s^2$ for Cd, and $5s^2$, $5p^3$ for Sb. The lattice structure relaxations are carefully performed so that the forces on atoms are smaller than 0.2 meV/Å, in which the conjugate gradient algorithm is utilized.

Starting from the experimental crystallographic coordinates³⁰ the crystal lattice parameters were optimized, computing the energy vs. volume curves of both compounds and fitting the Vinet equations of state.⁴¹ The electronic transport properties (e.g Seebeck coefficient and electrical conductivity) were calculated by solving the semiclassical Boltzmann transport equation assuming constant relaxation time approximation (CRTA) as implemented in the BoltzTrap package,⁴² using band energies obtained from WIEN2K electronic structure calculation as input. A dense mesh of $31 \times 8 \times 16$ k-points in the irreducible wedge of the Brillouin zone was used to obtain converged results.

Vibrational analysis and phonon dispersion curves were computed using the plane wave pseudopotential approach, as implemented in the VASP package,⁴³ with projector-augmented-

wave pseudopotentials.⁴⁴ GGA+U applied for frozen phonon calculations are based on the approach by Dudarev et al. as implemented in VASP.⁴⁵ Phonon dispersion curves, speed of sounds calculations and phonon density of states are obtained using the supercell frozen phonon method and the phonopy code.⁴⁶

Speed of Sound Measurements. Speed of sound measurements are performed using an Olympus 5072PR Pulser/Receiver system with a gain of 20dB and a 5kHz signal. Both longitudinal and shear measurements were made, using Olympus V112 (longitudinal) and Olympus V156 (shear) transducers and an Atten ADS 1102 oscilloscope.

Hall Measurements. Hall effect and resistivity measurements are performed using the Van der Pauw geometry on home-built apparatus.⁴⁷ Measurements are conducted up to 523 K under dynamic vacuum ($<10^{-4}$ Torr). Contacts are pressure-assisted nichrome wire.

RESULTS/DISCUSSION

Powder X-ray Diffraction and Sample Purity.

The Yb_2CdSb_2 structure type crystallizes in the noncentrosymmetric space group $Cmc2_1$ and has been well described by previous publications.^{29, 30} Ball-milling of elements followed by spark plasma sintering (SPS) resulted in samples with densities greater than 90% of theoretical values. Figure 2 shows the powder X-ray diffraction (PXRD) patterns of ground pellets of $\text{Yb}_{2-x}\text{Eu}_x\text{CdSb}_2$ ($x = 0.36, 0.85, 1.13, \text{ and } 1.18$, determined from EMPA provided below) compared to the calculated pattern for Yb_2CdSb_2 (top). Black asterisks indicate small impurity peaks that could not be indexed to this structure type or identified as a known phase. Since this is a consistent impurity for the series, we expect this study will provide insight to the intrinsic properties of the system.⁴⁸ Samples show a gradual left-shift in peak position with increasing x as unit cell parameters increase, consistent with Eu being incorporated into the structure primarily in the Yb1 six-coordinate site (Figure 1(b)) as Eu^{2+} has a larger ionic radius than Yb^{2+} (1.14 Å and 1.03 Å, respectively⁴⁹). Single crystal X-ray diffraction refinement from $\text{Yb}_{2-x}\text{Eu}_x\text{CdSb}_2$ indicate that Eu^{2+} prefers the Yb1 site, consistent with these results.^{29, 30} The Yb1 site,

with its greater average bond distance of 3.338 Å accommodates the larger Eu^{2+} more easily than the Yb2 site with its average bond distance of 3.168 Å. Lattice parameters extracted from whole-pattern fitting show increasing unit cell volume with increasing Eu concentration as expected, in good agreement with lattice parameters reported from single crystal X-ray diffraction results (ESI).^{29, 30} No further Rietveld analysis was employed due to significant peak broadening, likely from strain stemming from the ball-milling process as well as the high force applied by the SPS process.

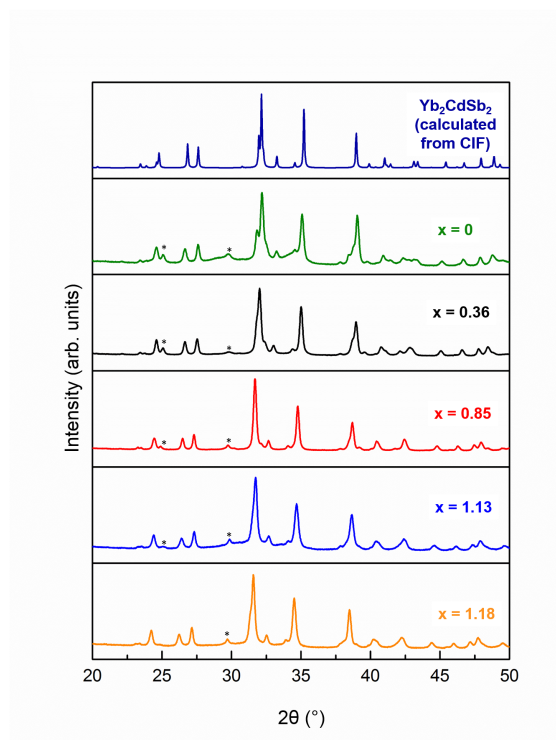


Figure 2(a): Powder X-ray Diffraction (PXRD) patterns for synthesized samples, $\text{Yb}_{2-x}\text{Eu}_x\text{CdSb}_2$. Black asterisks indicate an impurity unable to be indexed by PXRD. Whole pattern fitting for $x = 0, 0.36, 0.85, 1.13$ and 1.18 revealed unit cell volumes of $581 \text{ \AA}^3, 586 \text{ \AA}^3, 600 \text{ \AA}^3, 607 \text{ \AA}^3$, and 610 \AA^3 , respectively.

EMPA was used to verify stoichiometry and qualify the element homogeneity (EMPA images can be found in ESI). The average compositions of samples as determined by wavelength dispersive spectroscopy (WDS) are shown in Table 1. These results indicate that the $\text{Yb}_{2-x}\text{Eu}_x\text{CdSb}_2$ phase was formed in each case. Results are also in relatively good agreement with the preparative amounts of Eu and Yb and show, within error, that the total cation count is near 2 in all samples. The experimental value of x is employed to identify samples throughout.

Table 1: Sample compositions of $\text{Yb}_{2-x}\text{Eu}_x\text{CdSb}_2$ as determined by electron microprobe analysis (EMPA).

Preparative Eu Amount	Experimental Eu Amount	Sample Composition (As determined by EMPA)	Total Cation Count (Eu+Yb)
0.3	0.36	$\text{Yb}_{1.58(2)}\text{Eu}_{0.36(1)}\text{Cd}_{1.03(3)}\text{Sb}_{2.017(7)}$	1.94(2)
0.8	0.85	$\text{Yb}_{1.18(6)}\text{Eu}_{0.85(3)}\text{Cd}_{0.98(1)}\text{Sb}_{1.98(3)}$	2.03(3)
1	1.13	$\text{Yb}_{0.98(7)}\text{Eu}_{1.13(7)}\text{Cd}_{0.89(11)}\text{Sb}_{1.99(4)}$	2.11(10)
1.1	1.18	$\text{Yb}_{0.87(4)}\text{Eu}_{1.18(3)}\text{Cd}_{0.93(6)}\text{Sb}_{2.01(1)}$	2.05(6)

Electronic Structure

Yb_2CdSb_2 is a valence precise compound that can be described by the Zintl formalism. In a simple Zintl picture, Yb^{2+} donates two electrons to the more electronegative atoms, as confirmed by magnetic measurements.²⁹ The $[\text{CdSb}_2]^{4-}$ layers can be considered as composed of Cd^{2+} and Sb^{3-} , thus, $[\text{Yb}^{2+}]_2[\text{Cd}^{2+}][\text{Sb}^{3-}]_2$ is considered to be a charge balanced,⁵⁰ narrow-gap semiconductor. Density functional theory (DFT) calculations were employed to provide insight into the electronic structure, electronic transport and vibrational properties of these materials.

a. Crystal Structure

Electronic structure calculations were performed for two stoichiometric configurations of $\text{Yb}_{2-x}\text{Eu}_x\text{CdSb}_2$ with $x = 0$ and 1. Consistent with experimental structural analysis, the calculations support the preference of Eu substitution in the Yb1 site. In fact, a stable crystal structure could not be found when placing Eu in the Yb2 site. Theoretical lattice parameters are in good agreement with experiments (see Table S1 in the ESI). In particular, the calculated volume of Yb_2CdSb_2 (586 \AA^3) is within 1.6% of the experimental estimate (577 \AA^3). For $x = 1$ Eu substitution induces a significant volume expansion due to larger radius of Eu^{+2} (calculated: 620 \AA^3 ; experimental: 607 \AA^3). Electronic structure and electronic transport property calculations were performed using fully optimized crystal structures.

b. Electronic Structure

Spin polarized density functional theory calculations show that Yb_2CdSb_2 is nonmagnetic, as expected due to the presence of closed shell Yb^{+2} ($4f^{14}$), whereas the magnetic moment of YbEuCdSb_2 stems from the Eu $4f$ orbitals.²⁹ Eu^{+2} in the crystal retains its atomic magnetic

moment ($6.94 \mu_B$ in the atomic sphere) of 7 unpaired electrons, suggesting that $4f$ orbitals are inert and neither participate in chemical bonding nor in the Fermi level states involved in charge transport. We show below that this picture is oversimplified.

The band structure of Yb_2CdSb_2 is shown in Figure 3(a), and both spin-up (solid line) and spin-down (dotted line) bands of $\text{Yb}_{2-x}\text{Eu}_x\text{CdSb}_2$ ($x = 1$) are shown in Figure 3(b). The valence band maximum occurs at the Γ point while the conduction band minimum occurs at the Y symmetry point, yielding an indirect band gap (92 meV) in Yb_2CdSb_2 . This finding of a gap differs from the report of Xia and Bobev [Ref. 30], who used the augmented spherical wave method that applies spherical averages to potential and density within the atom sphere. Also not applied in Ref. 30 were the on-site repulsive interactions on Yb. The distinction results in our obtaining a band gap, and in placing the Yb $4f$ levels at -1.9 eV in our calculation, whereas their result had the center of the Yb $4f$ bands centered at -0.2 eV, leading to strong hybridization with the conduction bands up to the hole chemical potential at the higher hole concentrations.

The calculated band gap opens slightly to 111 meV for YbEuCdSb_2 . While band gaps calculated with DFT may be underestimated, the opening of the gap with increasing Eu concentration is consistent with the literature and experimental results presented below. Band gaps calculated from maximum Seebeck coefficient ($E_g = 2eS_{max}T_{max}$) in YbCd_2Sb_2 and EuCd_2Sb_2 ⁵¹ and with band structure calculations for YbMg_2Bi_2 and EuMg_2Bi_2 provide a similar trend.⁵² In both compounds the flat lanthanide f bands within the band structure can be clearly identified. In Yb_2CdSb_2 the valence band edge contains one roughly isotropic band, with a second band lying around 150 meV higher binding energy. An enlarged view is provided in Figure 3(c). The valence band edge is very similar for both compounds, but the spin down channel in Figure 3(b) reveals an exchange splitting of 0.5 eV reflecting the exchange coupling between Eu $4f$ and $5d$ orbitals. The half filled $4f$ orbitals provide an additional magnetic scattering mechanism when Eu is substituted into Yb_2CdSb_2 .

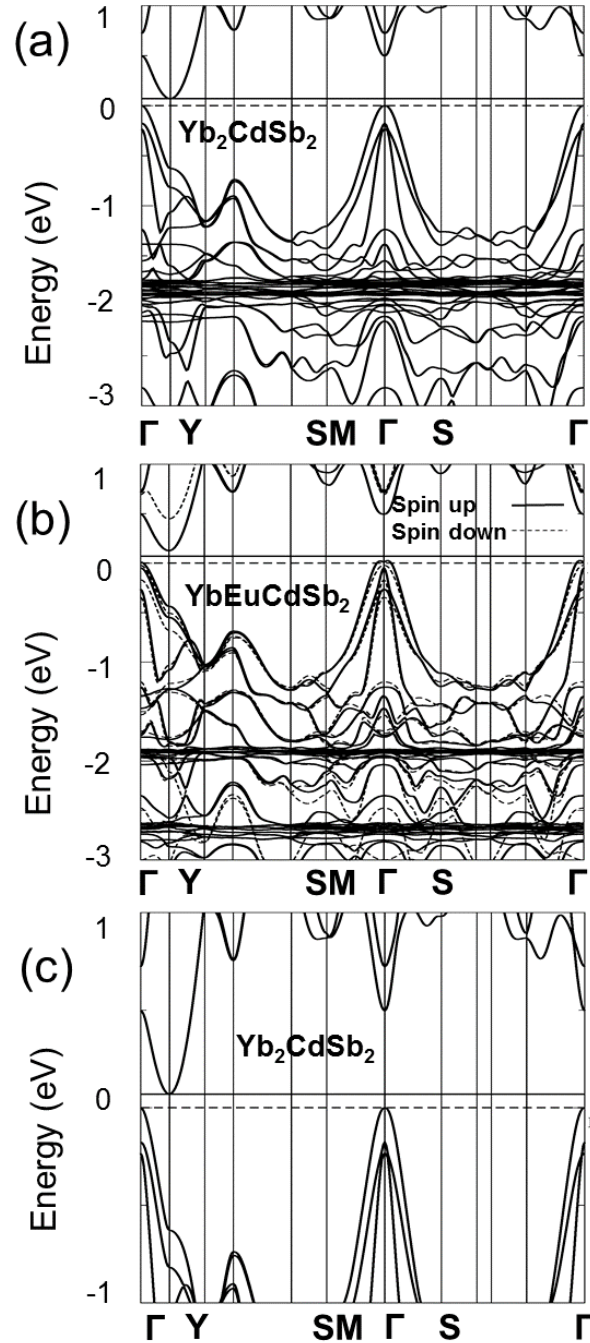


Figure 3: Band structure of $\text{Yb}_{2-x}\text{Eu}_x\text{CdSb}_2$ with valence (dashed) and conduction (solid) bands indicated (a) for $x = 0$, and (b) for combined spin majority (solid line) and spin minority (dashed line) bands for $x = 1$. Panel (a) shows flat bands at -1.9 eV from Yb $4f$ states whereas (b) shows flat bands around -1.9 eV arising from Yb $4f$ complemented with Eu $4f$ bands at -2.6 eV. Panel (c) presents an enlargement of the $x = 0$ band in (a) near the band gap.

The projected density of states (PDOS, Figure 4) for both $x = 0$ and $x = 1$ show that the main character of the valence band is dictated by Sb $5p$ states, with Sb p , Cd p and Yb f orbitals contributing at higher hole binding energy. In both compounds, Sb $5p$, Cd $5p$, lanthanide $5d$

electrons are the majority participants in covalent bonding in the valence band (see more details in Figure S7 in ESI). While the band structure (Figure 3) might suggest little interaction of the f orbitals, the PDOS reveals Yb f character rising rapidly a few tenths of eV below the gap. In the $x = 1$ compound the f bands of Eu, which lie -2.6 eV below the gap, push the Yb f character near the gap to higher energy, thus accentuating the f character of holes doped into the valence band. Such doping-induced changes in the PDOS are small enough not to produce major changes in hole mobility, but dictate the different trends in the Seebeck coefficient computed for pure and Eu-doped Yb_2CdSb_2 .

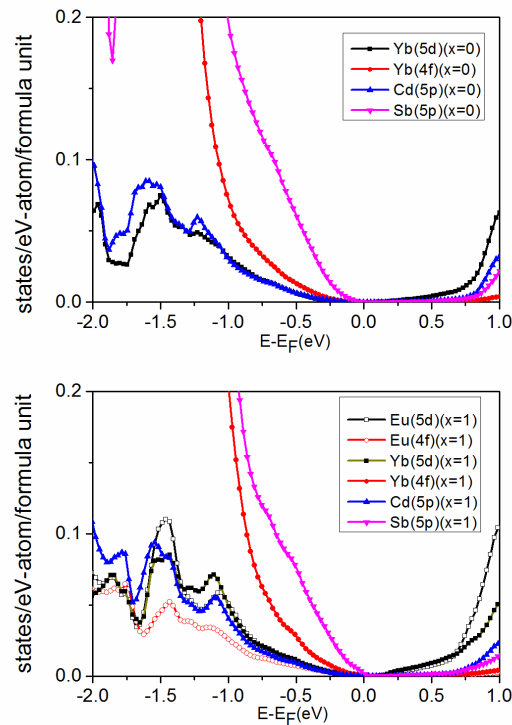


Figure 4: Orbital-projected density of states plot using the DFT+U functional for $\text{Yb}_{2-x}\text{Eu}_x\text{CdSb}_2$. (a) Participating atomic orbitals near the valence edge are shown for $x = 0$. (b) All participating orbitals near the valence edge are shown for $x = 1$. The majority spin channel is shown for $x = 1$ in these plots. Additional detailed PDOS plots are provided in ESI.

Electronic Transport Properties.

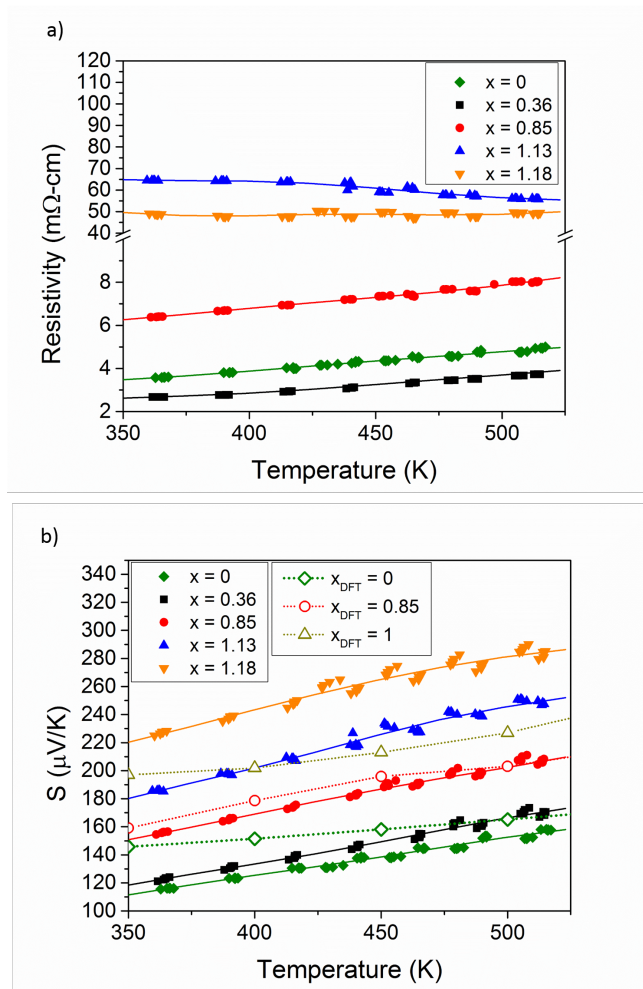


Figure 5: Temperature dependent (a) electrical resistivity and (b) Seebeck coefficient on polycrystalline samples of $\text{Yb}_{2-x}\text{Eu}_x\text{CdSb}_2$. The calculated Seebeck coefficients (open symbols) use experimental carrier (hole) concentration from Table 2. For $x = 1$ the carrier concentration is obtained by interpolating between the experimental carrier concentrations at $x = 0.85$ and $x = 1.13$. Experimental data points are shown as filled symbols and fits as solid lines.

Based on Zintl valence-counting rules and consistent with the DFT-calculated band structure calculations, stoichiometric $\text{Yb}_{2-x}\text{Eu}_x\text{CdSb}_2$ compounds are expected to show semiconducting behavior. The electrical resistivities (Figure 5a) of $x = 0, 0.36$ and $x = 0.85$ samples are small and show metallic temperature dependences, as in degenerate semiconductors, while $x = 1.13$ and $x = 1.18$ show higher resistivity, consistent with both the widening of the band gap and the lowered carrier concentrations. The transition from degenerate to non-degenerate behavior seen in electrical resistivity is reflected in Seebeck measurements, as it would be expected that metallic systems have lower Seebeck coefficients. $S(T, x)$ increases monotonically with Eu concentration, correlating with the system becoming less metallic. Hole concentrations at 323 K (

Table 2) are in the range of $\sim 10^{19}$ due to intrinsic and compositional defects. Increasing Eu concentration causes the hole concentration to decrease, possibly because there are more defects on Yb sites, as it has been seen in other cases of Eu substitution for Yb.^{53, 54} This is consistent with the cation totals seen in the composition (Table 1). According to the Nagle electronegativity scale,⁵⁵ Yb is more electronegative than Eu which has been suggested to influence carrier concentration because of incomplete electron donation from the cation.⁵⁴ The 373 K mobility data (Table 2) show high values for $x = 0, 0.36$ and 0.85 , not often seen in Zintl phases, and sharply decreases for $x = 1.13$ and $x = 1.18$. Additional Hall data are provided in the ESI.

Table 2: Carrier (hole) concentration and mobility data for each sample composition, $\text{Yb}_{2-x}\text{Eu}_x\text{CdSb}_2$ at 323 K.

Eu Concentration (x)	Carrier Concentration (n)(cm^{-3})	Mobility (cm^2/Vs)
0	$4.53 \cdot 10^{19}$	70.30
0.36	$3.56 \cdot 10^{19}$	72.18
0.85	$8.96 \cdot 10^{18}$	95.93
1.13	$5.37 \cdot 10^{18}$	24.55
1.18	$1.41 \cdot 10^{19}$	17.51

The $x = 0.36$ phase shows the highest carrier concentration. From this, we can propose that Yb vacancies are the major source for charge carriers (total cation stoichiometry is less than 2, Table 1), and substituting the Yb site with other alio- and isovalent cations can be a useful tool for band engineered thermoelectrics. The non-monotonous mobility is one of the key subjects of interest of further investigation.

Experimental temperature dependent Seebeck coefficients are shown in Figure 5(b) (filled symbols). All are positive in the entire range, indicative of holes as the dominant charge carriers. Consistent with previous studies on single crystal samples, the Seebeck is large in all samples. The Seebeck coefficient increases with Eu concentration, reaching a maximum value of $\sim 270 \mu\text{V/K}$ for the $x = 1.18$ phase at 523 K. Each sample shows nearly linear temperature dependence, typical of heavily doped semiconductors. Additionally, theoretically computed

Seebeck coefficients are plotted in Figure 5b (open symbols) for $x = 0, 0.85,$ and 1 . To compare to experiments, which are performed on polycrystalline samples, S is defined as $1/3$ of the trace of the anisotropic Seebeck tensor of a single crystal. For these calculations, the experimentally determined carrier concentrations (Table 2) were used, and for the $x = 1$ compound the carrier concentration was interpolated from the experimental data at $x = 0.85$ and 1.13 . To compute the Seebeck coefficient of $\text{Yb}_{1.15}\text{Eu}_{0.85}\text{CdSb}_2$ the band structure of YbEuCdSb_2 was employed. Theory and experiments for this system exhibit excellent agreement, which suggests all electron based DFT+U level of calculations and the semiclassical Boltzmann transport equation in CRTA can provide a faithful prediction of Seebeck coefficients for the $\text{Yb}_{2-x}\text{Eu}_x\text{CdSb}_2$ (2-1-2) Zintl family.

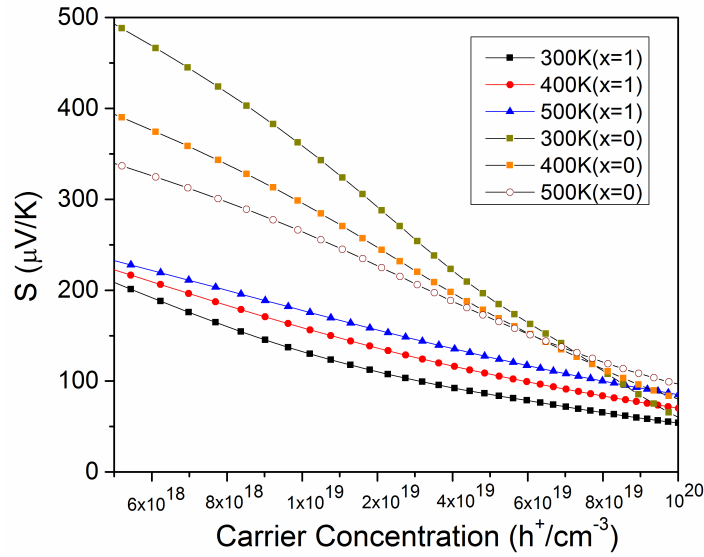


Figure 6: Dependence of the Seebeck coefficients on carriers (holes) concentration for $\text{Yb}_{2-x}\text{Eu}_x\text{CdSb}_{11}$ ($x = 0, 1$). For $x = 0$ configuration, a temperature dependent crossover is observed near $7 \times 10^{19} \text{ cm}^{-3}$.

The effect of carrier concentration (n) on the calculated Seebeck coefficients is shown in Figure 6, which reveals that Yb_2CdSb_2 exhibits a crossover in its temperature dependence, at $n \sim 7 \cdot 10^{19} \text{ cm}^{-3}$. Below this value, the Seebeck coefficient decreases with increasing temperature, while at larger n the Seebeck coefficients become proportional to the temperature. This is the finger print of a transition from a non-degenerate to a degenerate semiconductor. For YbEuCdSb_2 $S(T)$ is proportional to the temperature irrespective of carrier concentration. All experimental samples

follow the trend of YbEuCdSb₂ shown in Figure 6, so even the smallest amount of Eu substituted into the structure leads to $S(T)$ that trends according to YbEuCdSb₂ (Yb_{2-x}Eu_xCdSb₂, $x = 1$ model). From the calculation of the electrical transport coefficients of Yb₂CdSb₂ and YbEuCdSb₂ in CRTA we can infer the ratio between the electrical resistivity (ρ) of the two systems at the same n , without making any assumption on the carrier lifetime. Since ρ is inversely proportional to the effective mass (m^*) we can also estimate the change in m^* upon Eu doping. We also calculated valence band effective mass m^* from the second derivative of band dispersion curve along the Γ -Y, Γ -SM and Γ -S directions (Figure 3 (a)-(c)). Since both Yb_{2-x}Eu_xCdSb₂ ($x = 0, 1$) exhibit multivalley band dispersion along three different band directions, we calculated the average (geometric mean) m^* along these three directions. The results are $m^* = 0.33$ and 0.36 for the $x = 0, 1$ phases, respectively. Such small difference in m^* suggests that the changes observed in the transport coefficients as a function of Eu concentration are dictated by the carrier concentration.

The small changes in hole mobility, which stems from the valence band edge being relatively insensitive to Eu alloying, suggest that co-doping with other elements to achieve a disordered Zintl phase might be used to engineer a higher Seebeck and possibly better zT , as observed for Ca doping in (Eu_{0.5}Yb_{0.5})_{1-x}Ca_xMg₂Bi₂.⁵⁶

Thermal Transport Properties.

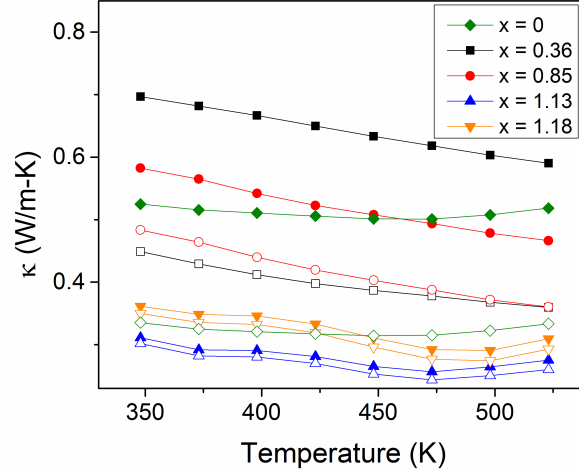


Figure 7: Total and lattice thermal conductivity of $\text{Yb}_{2-x}\text{Eu}_x\text{CdSb}_2$. Total thermal conductivity is shown as solid symbols and lattice thermal conductivity is shown as open symbols.

The total thermal conductivity, shown in Figure 7, is calculated from the thermal diffusivity (D). The DFT calculated heat capacity of Yb_2CdSb_2 (ESI) yields a value of 0.17 J/g-K , in good agreement with values predicted by the Dulong-Petit model as well as experimentally measured C_p . The calculated thermal conductivity is extremely low and comparable to other systems with anomalously low κ_T such as coinage metal-stuffed $\text{Eu}_9\text{Cd}_4\text{Sb}_9$ ⁹ and $\text{Yb}_2\text{Mn}_{4.2}\text{Sb}_9$.⁵⁷ The total thermal conductivity (κ_T) is a combination of lattice (κ_L) and electronic (κ_e) contributions. κ_e can be estimated using the Wiedemann-Franz relation ($\kappa_e = LT/\rho$). Here, L was calculated using equation 2⁵⁸, assuming a single parabolic band (SPB) model and primarily acoustic phonon scattering. L values are shown in the ESI.

$$L = 1.5 + \exp\left(\frac{-S}{116}\right) \quad (2)$$

In all systems, κ_e is small and subtracting it from κ_T yields κ_L (ESI), the main contributor to κ_T . Cahill *et al.*⁵⁹ proposed an empirical expression for the theoretical minimum for κ_L as:

$$\kappa_{min} = \frac{1}{2} \left(\frac{\pi}{6}\right)^{1/3} \frac{k_B}{V^{2/3}} (2v_T + v_L) \quad (3)$$

where k_B is the Boltzmann constant, V is the average volume per atom, and v_T and v_L are the transverse and longitudinal speeds of sound, respectively. κ_{min} values are calculated for each composition and shown compared to κ_L and, in each composition, κ_L falls below its theoretical minimum. In a physical description, κ_L cannot be lower than κ_{min} and it can be inferred that the SPB model is inadequate or there are scattering mechanisms other than acoustic phonon scattering that are present (*e.g.* ionized impurity scattering) that yield unphysical values of L .

Regardless, κ_T is extremely low at these near ambient temperatures, comparable to or lower than other materials^{57, 60, 61} at high temperatures where κ_T should be at its lowest, and makes this a promising system for thermoelectric applications.

Such low κ_T values are not necessarily expected in such a simple structure. Similarly, PbTe, a simple rocksalt structure with no nanoinclusions, complex unit cell or ‘rattler’ atoms, yielded an inexplicably low κ_T (~ 2 W/m-K). This was attributed to avoided crossing in the phonon band structure and softening of certain branches generating soft lattice behavior.⁶² To elucidate the possible origin of the low thermal conductivity of these compounds, the phonon band structure for $x = 0$ was calculated and is shown in Figure 8. The unit cell of Yb_2CdSb_2 contains 20 atoms, yielding 3 acoustic and 57 optical branches. The acoustic modes are confined to low frequency, below 2 THz (~ 8.3 meV), with low group velocities over the whole Brillouin zone. Optical branches start as low as 0.7 THz (~ 2.9 meV) and intersect with acoustic branches providing a large density of 3-phonon scattering channels. The optical bands have very low group velocities, thus contributing very little to the overall thermal conductivity. These features work in tandem to lower the lattice thermal conductivity of the compound, as has been seen in other Cd based Zintl compounds, especially in the antimonides.⁶³

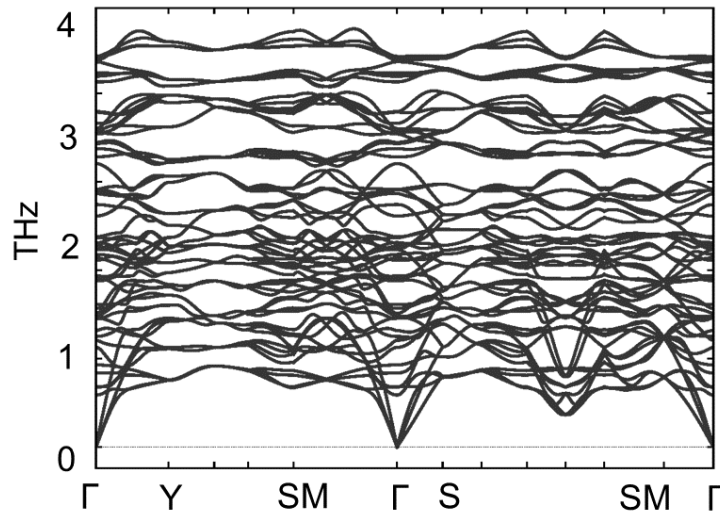


Figure 8: Phonon dispersion of $\text{Yb}_{2-x}\text{Eu}_x\text{CdSb}_2$ $x = 0$ by frozen phonon approximation, all optical bands are very flat in nature.

The lattice thermal conductivity can be expressed in the following equation:

$$\kappa_L = v_s c_s l_{ph} \quad (4)$$

where v_s is the phonon group velocity, c_s is the speed of sound, and l_{ph} is the phonon mean free path. According to equation (4), thermal conductivity is proportional to the speed of sound in the material. The computed longitudinal group velocity for Yb_2CdSb_2 along three different crystallographic axes (a , b and c) provides speeds of sound along different axes values: 3520 m/s (a), 2644 m/s (b), 2671 m/s (c). By taking the average value of above three velocities, 2900 m/s as longitudinal speed of sound is obtained. The transverse (shear) phonon mode yields 1878 m/s (a), 2163 m/s (b), 2105 m/s (c) and 2048 m/s as an average. These values are in good agreement with the experimental values (Table 3) and support the decreasing thermal conductivity with increasing Eu incorporation as this would increase point scattering throughout the system.

Additionally, as aforementioned, Eu preferentially substitutes on the interlayer site between polyanionic sheets. As the Eu concentration surpasses unity in $x = 1.13$ and 1.18 , Eu is also found on the intralayer site²⁹ and stretches out the accordion-like polyanionic units. This yields disorder and strain in the lattice, further lowering thermal conductivity as can be seen by the discontinuity in κ_T between $x = 0.85$ and $x = 1.13$. Experimentally determined speeds of sound (Figure 9) support this conclusion as these values are comparable to other materials with low thermal conductivity,^{9, 57} decreasing with increasing Eu concentration. Speed of sound values suddenly make a dramatic drop at $x = 1.13$, further supporting the idea that the additional Eu on the intralayer site significantly affects the lattice. Thus, it can be concluded that the site specific substitution, alloy scattering, and lack of center of symmetry in this structure type lead to the low sound velocity and significant phonon-phonon scattering that are the origins of the extremely low κ_L .

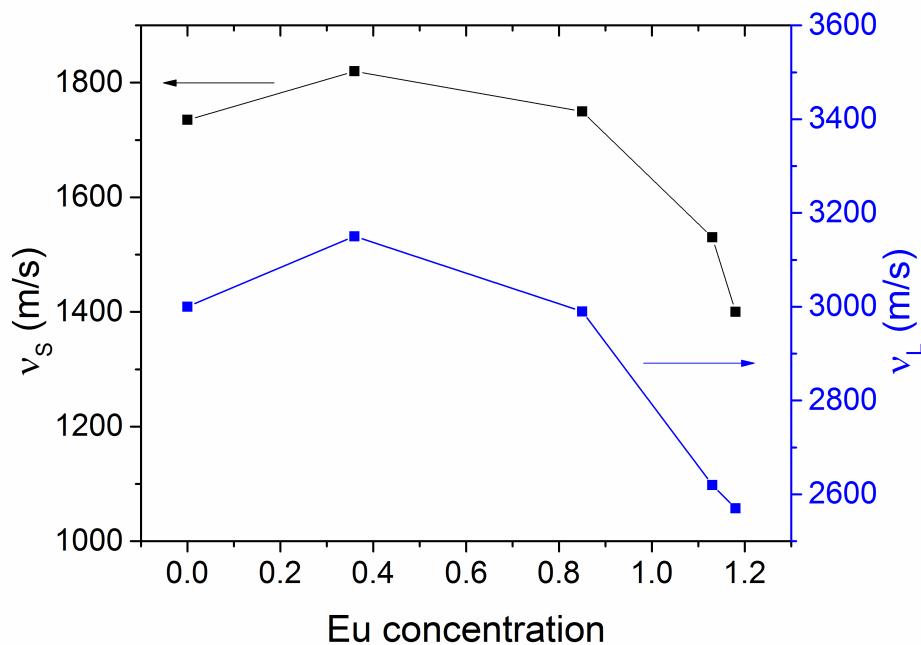


Figure 9: Shear and longitudinal speeds of sound for each sample. Speed of sound data are tabulated in Table S2 of the ESI.

Figure of Merit.

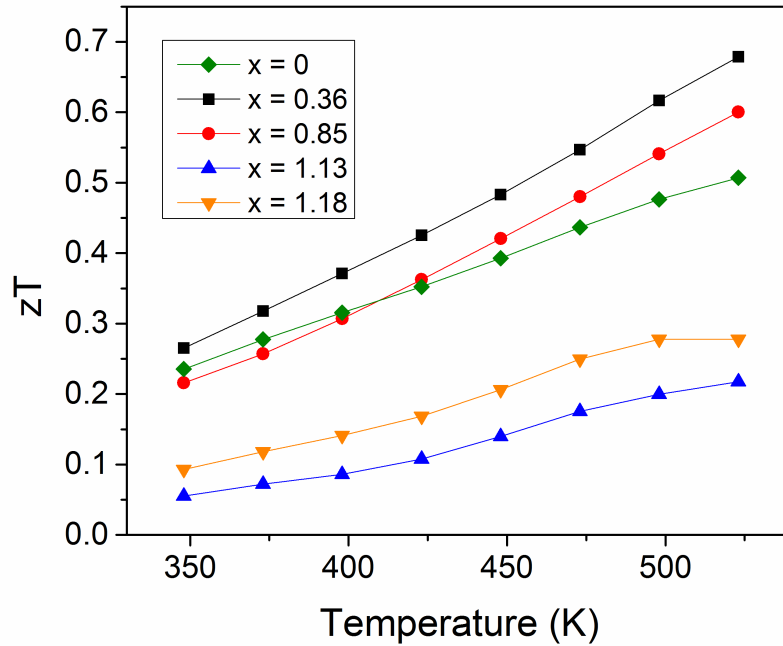


Figure 10: The calculated figure of merit of $\text{Yb}_{2-x}\text{Eu}_x\text{CdSb}_2$.

The figure of merit of $\text{Yb}_{2-x}\text{Eu}_x\text{CdSb}_2$ ($x = 0.36, 0.85, 1.13, 1.18$) is shown in Figure 10 as a function of temperature. All zT curves increase with temperature to 523 K with decreasing zT as Eu concentration increases. The reduction of zT is due to the large increase in electrical resistivity rendered upon having concentrations of Eu equal to or greater than that of Yb in the structure. The $x = 0.36$ composition of $\text{Yb}_{2-x}\text{Eu}_x\text{CdSb}_2$ shows near optimal carrier concentration and good mobility making it the best in this series for moderate to low temperature applications, as the zT curve for $x = 0.36$ is slightly greater than that of TAGS, a well known moderate temperature thermoelectric material.⁶⁴ Overall, $x = 0.36$ reaches a maximum zT of ~ 0.7 at 523 K, an excellent temperature range for waste heat recovery such as in the case of mid-temperature STEGs. However, the thermal conductivity is not the lowest for this composition, suggesting that further tuning of the 2-1-2 family can lead to increased efficiency.

CONCLUSION.

In this paper we have described a promising thermoelectric structure type, $\text{Yb}_{2-x}\text{Eu}_x\text{CdSb}_2$, with favorable thermoelectric properties. Band structure calculations reveal the compounds to be indirect band gap semiconductors with a band gap that increases with Eu concentration. Though

their band centers lie well below the gap, the *f* orbitals of Yb influence somewhat the values of the Seebeck coefficients through hybridization in states just below the gap, contributing to the high Seebeck coefficients observed in these compounds. Complexities in the phonon dispersion along with point defect scattering from Eu substitution allow for very low thermal conductivity. This paired with low electrical resistivity in Yb_{1.7}Eu_{0.3}CdSb₂ results in high *zT* of ~0.7 at 523 K. These results represent an initial set of measurements that guide our understanding of how to optimize this system further. The very low thermal conductivity of the series is optimized, as the lattice contribution (the major contribution to thermal conductivity) is at or below the theoretical minimum, and further efforts to improve *zT* can be focused on improving electrical transport properties either through controlling carrier concentration (*e.g.* aliovalent doping), as *zT* could likely be greater with higher carrier concentration, or through enhancing thermopower (*e.g.* band engineering). Further efforts of substituting on the rare earth sites of Yb_{2-x}EuCdSb₂ with nonmagnetic group I or group II materials may provide a higher Seebeck coefficient and increase *zT* further.

Conflicts of Interest. There are no conflicts of interest to declare.

Acknowledgements. We thank Nicholas Botto for microprobe analysis, GAANN (J.C.), and NSF DMR—1405973, -1709382 and NSF CAREER award DMR-1555340 for funding. W.E.P was supported by DOE NNSA grant DE-NA0002908. The National Energy Research Scientific Computing Center (NERSC), a DOE Office of Science User Facility supported by the Office of Science of the U.S. Department of Energy under Contract No. DE-AC02-05CH11231, as well as an in-house computational cluster at the University of California Davis are gratefully acknowledged.

REFERENCES

1. J. Yang and F. R. Stabler, *Journal of Electronic Materials*, 2009, **38**, 1245-1251.
2. D. Kraemer, B. Poudel, H.-P. Feng, J. C. Caylor, B. Yu, X. Yan, Y. Ma, X. Wang, D. Wang, A. Muto, K. McEnaney, M. Chiesa, Z. Ren and G. Chen, *Nat Mater*, 2011, **10**, 532-538.
3. A. S. Glen, in *CRC Handbook of Thermoelectrics*, CRC Press, 1995, DOI: 10.1201/9781420049718.ch34.
4. S. M. Kauzlarich, S. R. Brown and G. Jeffrey Snyder, *Dalton Transactions*, 2007, DOI: 10.1039/B702266B, 2099-2107.
5. S. R. Brown, S. M. Kauzlarich, F. Gascoin and G. J. Snyder, *Chemistry of Materials*, 2006, **18**, 1873-1877.
6. J. Cooley, N. Kazem, J. V. Zaikina, J. C. Fettinger and S. M. Kauzlarich, *Inorganic Chemistry*, 2015, **54**, 11767-11775.

7. K. Guo, Q. Cao and J. Zhao, *Journal of Rare Earths*, 2013, **31**, 1029-1038.
8. N. Kazem, W. Xie, S. Ohno, A. Zevalkink, G. J. Miller, G. J. Snyder and S. M. Kauzlarich, *Chemistry of Materials*, 2014, **26**, 1393-1403.
9. N. Kazem, J. V. Zaikina, S. Ohno, G. J. Snyder and S. M. Kauzlarich, *Chemistry of Materials*, 2015, **27**, 7508-7519.
10. B. Saparov, H. He, X. Zhang, R. Greene and S. Bobev, *Dalton Transactions*, 2010, **39**, 1063-1070.
11. E. S. Toberer, A. Zevalkink, N. Crisosto and G. J. Snyder, *Advanced Functional Materials*, 2010, **20**, 4375-4380.
12. A. Zevalkink, Y. Takagiwa, K. Kitahara, K. Kimura and G. J. Snyder, *Dalton Transactions*, 2014, **43**, 4720-4725.
13. J. Shuai, J. Mao, S. Song, Q. Zhang, G. Chen and Z. Ren, *Materials Today Physics*, 2017, **1**, 74-95.
14. J. Shuai, J. Mao, S. Song, Q. Zhang, G. Chen and Z. Ren, *Materials Today Physics*, 2017, **1**, 74-95.
15. Y. Hu, S. K. Bux, J. H. Grebenkemper and S. M. Kauzlarich, *Journal of Materials Chemistry C*, 2015, **3**, 10566-10573.
16. Y. Hu and S. M. Kauzlarich, *Dalton Transactions*, 2017, **46**, 3996-4003.
17. H. Tamaki, H. K. Sato and T. Kanno, *Advanced Materials*, 2016, **28**, 10182-10187.
18. A. Saramat, G. Svensson, A. E. C. Palmqvist, C. Stiewe, E. Mueller, D. Platzek, S. G. K. Williams, D. M. Rowe, J. D. Bryan and G. D. Stucky, *Journal of Applied Physics*, 2006, **99**, 023708.
19. P. Sundarraj, D. Maity, S. S. Roy and R. A. Taylor, *RSC Advances*, 2014, **4**, 46860-46874.
20. W. G. Zeier, A. Zevalkink, Z. M. Gibbs, G. Hautier, M. G. Kanatzidis and G. J. Snyder, *Angewandte Chemie International Edition*, 2016, **55**, 6826-6841.
21. W. Liu, J. Hu, S. Zhang, M. Deng, C.-G. Han and Y. Liu, *Materials Today Physics*, 2017, **1**, 50-60.
22. H. Kleinke, *Chemistry of Materials*, 2010, **22**, 604-611.
23. M. G. Kanatzidis, *MRS Bulletin*, 2015, **40**, 687-695.
24. A. J. Minnich, M. S. Dresselhaus, Z. F. Ren and G. Chen, *Energy & Environmental Science*, 2009, **2**, 466-479.
25. K. Takahata, Y. Iguchi, D. Tanaka, T. Itoh and I. Terasaki, *Physical Review B*, 2000, **61**, 12551-12555.
26. H. J. Goldsmid, *Proceedings of the Physical Society. Section B*, 1956, **69**, 203.
27. E. S. Toberer, A. F. May, B. C. Melot, E. Flage-Larsen and G. J. Snyder, *Dalton Transactions*, 2010, **39**, 1046-1054.
28. H. Zhang, M. Baitinger, M.-B. Tang, Z.-Y. Man, H.-H. Chen, X.-X. Yang, Y. Liu, L. Chen, Y. Grin and J.-T. Zhao, *Dalton Transactions*, 2010, **39**, 1101-1104.
29. B. Saparov, M. Saito and S. Bobev, *Journal of Solid State Chemistry*, 2011, **184**, 432-440.
30. S.-q. Xia and S. Bobev, *Journal of the American Chemical Society*, 2007, **129**, 4049-4057.
31. F. Serrano-Sánchez, M. Gharsallah, N. M. Nemes, F. J. Mompean, J. L. Martínez and J. A. Alonso, *Applied Physics Letters*, 2015, **106**, 083902.
32. L.-D. Zhao, S.-H. Lo, Y. Zhang, H. Sun, G. Tan, C. Uher, C. Wolverton, V. P. Dravid and M. G. Kanatzidis, *Nature*, 2014, **508**, 373-377.
33. J. Rodríguez-Carvajal, *Physica B: Condensed Matter*, 1993, **192**, 55-69.
34. P. Blaha, K. Schwarz, P. Sorantin and S. B. Trickey, *Computer Physics Communications*, 1990, **59**, 399-415.
35. G. K. H. Madsen, P. Blaha, K. Schwarz, E. Sjöstedt and L. Nordström, *Physical Review B*, 2001, **64**.
36. K. Schwarz, P. Blaha and G. K. H. Madsen, *Computer Physics Communications*, 2002, **147**, 71-76.
37. J. P. Perdew, K. Burke and M. Ernzerhof, *Physical Review Letters*, 1996, **77**, 3865-3868.
38. V. I. Anisimov, I. V. Solovyev, M. A. Korotin, M. T. Czyżyk and G. A. Sawatzky, *Physical Review B*, 1993, **48**, 16929-16934.
39. A. I. Liechtenstein, V. I. Anisimov and J. Zaanen, *Physical Review B*, 1995, **52**, R5467-R5470.

40. E. Flage-Larsen, S. Diplas, O. Prytz, E. S. Toberer and A. F. May, *Physical Review B*, 2010, **81**.
41. P. Vinet, Rose, J.H., Ferrante, J. and Smith, J.R., *Journal of Physics: Condensed Matter*, 1989, **1**.
42. G. K. H. Madsen and D. J. Singh, *Computer Physics Communications*, 2006, **175**, 67-71.
43. G. Kresse and J. Furthmuller, *Physical Review B*, 1996, **54**, 11169-11186.
44. G. Kresse and D. Joubert, *Physical Review B*, 1999, **59**, 1758-1775.
45. S. L. Dudarev, G. A. Botton, S. Y. Savrasov, C. J. Humphreys and A. P. Sutton, *Physical Review B*, 1998, **57**, 1505-1509.
46. A. Togo and I. Tanaka, *Scripta Materialia*, 2015, **108**, 1-5.
47. K. A. Borup, J. de Boor, H. Wang, F. Drymiotis, F. Gascoin, X. Shi, L. Chen, M. I. Fedorov, E. Muller, B. B. Iversen and G. J. Snyder, *Energy & Environmental Science*, 2015, **8**, 423-435.
48. S. Ohno, U. Aydemir, M. Amsler, J.-H. Pöhls, S. Chanakian, A. Zevalkink, M. A. White, S. K. Bux, C. Wolverton and G. J. Snyder, *Advanced Functional Materials*, 2017, **27**, 1606361-n/a.
49. Y. Q. Jia, *Journal of Solid State Chemistry*, 1991, **95**, 184-187.
50. *Chemistry, structure, and bonding of Zintl phases and ions*, VCH, New York ;, 1996.
51. *The Journal of Chemical Physics*, 2010, **133**, 194701.
52. J. Shuai, H. Geng, Y. Lan, Z. Zhu, C. Wang, Z. Liu, J. Bao, C.-W. Chu, J. Sui and Z. Ren, *Proceedings of the National Academy of Sciences*, 2016, **113**, E4125-E4132.
53. J. Shuai, Y. Wang, Z. Liu, H. S. Kim, J. Mao, J. Sui and Z. Ren, *Nano Energy*, 2016, **25**, 136-144.
54. G. S. Pomrehn, A. Zevalkink, W. G. Zeier, A. van de Walle and G. J. Snyder, *Angewandte Chemie*, 2014, **126**, 3490-3494.
55. J. K. Nagle, *Journal of the American Chemical Society*, 1990, **112**, 4741-4747.
56. J. Shuai, H. Y. Geng, Y. C. Lan, Z. Zhu, C. Wang, Z. H. Liu, J. M. Bao, C. W. Chu, J. H. Sui and Z. F. Ren, *Proceedings of the National Academy of Sciences of the United States of America*, 2016, **113**, E4125-E4132.
57. S. K. Bux, A. Zevalkink, O. Janka, D. Uhl, S. Kauzlarich, J. G. Snyder and J.-P. Fleurial, *Journal of Materials Chemistry A*, 2014, **2**, 215-220.
58. H.-S. Kim, Z. M. Gibbs, Y. Tang, H. Wang and G. J. Snyder, *APL Mater.*, 2015, **3**, 041506.
59. D. G. Cahill, S. K. Watson and R. O. Pohl, *Physical Review B*, 1992, **46**, 6131-6140.
60. A. Zevalkink, W. G. Zeier, G. Pomrehn, E. Schechtel, W. Tremel and G. J. Snyder, *Energy & Environmental Science*, 2012, **5**, 9121-9128.
61. A. Zevalkink, E. S. Toberer, W. G. Zeier, E. Flage-Larsen and G. J. Snyder, *Energy & Environmental Science*, 2011, **4**, 510-518.
62. O. Delaire, J. Ma, K. Marty, A. F. May, M. A. McGuire, M. H. Du, D. J. Singh, A. Podlesnyak, G. Ehlers, M. D. Lumsden and B. C. Sales, *Nat Mater*, 2011, **10**, 614-619.
63. T. Pandey and A. K. Singh, *Physical Chemistry Chemical Physics*, 2015, **17**, 16917-16926.
64. *NASA MMRTG Reference Data*.